Journal of Alloys and Compounds xxx (xxxx) 165762

Contents lists available at ScienceDirect

Journal of Alloys and Compounds

journal homepage: www.elsevier.com/locate/jallcom

Effects of transient thermal shock on the microstructures and corrosion properties of a reduced activation high-entropy alloy

Wei-Ran Zhang [a, b], Wei-Bing Liao [c, *], Peter K. Liaw [d], Jing-Li Ren [e], Jamieson Brechtl [f], Yong Zhang [b, g, *]

[a] Xi'an Rare Metal Materials Institute Co. Ltd, Xi'an 710016, China
[b] School of Mechanical Engineering, Qinghai University, Xining 810016, China
[c] Key Laboratory of Optoelectronic Devices and Systems of Ministry of Education and Guangdong Province, College of Physics and Optoelectronic Engineering, Shenzhen University, Shenzhen 518060, China
[d] Department of Materials Science and Engineering, The University of Tennessee, Knoxville, TN 37996, USA
[e] Henan Academy of Big Data, Zhengzhou University, Zhengzhou 450052, China
[f] Energy and Transportation Sciences Division, Oak Ridge National Laboratory, Oak Ridge, TN 37831, USA
[g] Beijing Advanced Innovation Center of Materials Genome Engineering, State Key Laboratory for Advanced Metals and Materials, University of Science and Technology Beijing, Beijing 100083, China

ARTICLE INFO

Article history:
Received 29 January 2022
Received in revised form 26 May 2022
Accepted 1 June 2022

Keywords:
High-entropy alloy
Transient thermal shock
Microstructure
Corrosion resistance
Refined composite multiscale entropy

ABSTRACT

The devices would subject transient thermal shocks (TTS) during operation under extremely harsh conditions of nuclear fusion reactors, which inevitably exert significant impact on the microstructure and performance of structural materials. In this work, a reduced activation $VCrFeTa_{0.2}W_{0.2}$ high-entropy alloy (HEA) was developed by vacuum arc melting. The effects of electron beam induced TTS on its microstructure, microhardness, and corrosion properties were investigated. The results indicate that the weight fraction of each phase changes after TTS, showing a significant decrease in the content of BCC1 phase and an increase in the content of BCC2 and Laves phases. The content of BCC1 phase continues to decrease slightly with increasing the power of TTS. Besides, the microhardness of the alloy increases from ~673 HV to ~714 HV after TTS treatments. In the reduced activation HEA, TTS results in a relatively low corrosion current density of ~0.472 μA/cm^2 in 3.5 wt% NaCl solution, around one-third of the current density observed in the as-cast sample. Furthermore, the $VCrFeTa_{0.2}W_{0.2}$ HEA after TTS exhibits a pitting potential of ~1.165 V_{SCE}, which is much higher than that of the as-cast sample. The refined composite multiscale entropy method is employed to analyze the influence of TTS on current fluctuation behavior during the corrosion process. The reduced activation $VCrFeTa_{0.2}W_{0.2}$ HEA exhibits excellent properties in harsh environments after TTS, thereby showing advantageous property in the field of nuclear structural materials. Moreover, TTS is an efficient and controllable strategy for the improvement of the HEAs' microstructures and performances.

© 20XX

1. Introduction

High-entropy alloy (HEA) shows great potential in the future nuclear structural materials owing to its excellent mechanical and physical properties, such as high yield strength, irradiation resistance and excellent ductility [1–5]. It was reported that the compositional complexity exerted a large effect on ion-irradiation induced swelling and hardening in HEAs [6]. The HEAs exhibit excellent resistance to radiation damage under heavy ion bombardment, as well as high resistance to helium bubble formation, compared to W, Ni and steel [7–10], indicating that HEAs are ideal structural materials under extreme irradiation conditions.

The plasma-facing materials (PFMs) used in the first wall of nuclear fusion devices suffer extreme thermal radiation during operation. It is reported that the PFMs are subjected to a quasi-stationary heat load of 10 MW•m^{-2} and a slow transient heat load of 20 MW•m^{-2} [11,12], which could cause thermal fatigue, cracking, and melting of PFMs [13–19]. Therefore, a harsh service environment in transient thermal shock (TTS) in a nuclear reactor would severely limit the lifetime of PFMs [11,16,20,21]. Over the past decades, tungsten and its compos-

* Corresponding author.
* Corresponding author at: School of Mechanical Engineering, Qinghai University, Xining 810016, China.
E-mail addresses: liaowb@szu.edu.cn (W.-B. Liao), drzhangy@ustb.edu.cn (Y. Zhang).

https://doi.org/10.1016/j.jallcom.2022.165762
0925-8388/© 20XX

CORRECTED PROOF

Note: Low-resolution images were used to create this PDF. The original images will be used in the final composition.

ites have been considered as one of the most promising PFMs candidates for fusion reactors due to their excellent physical and chemical properties, such as high melting point and thermal conductivity, low sputtering yield and tritium retention [11,15,17,20–23]. However, repeated electron irradiations may lead to obvious surface roughening, cracks, and extruded structure in W–Zr/Sc_2O_3 composites [24]. Commercial bulk W exhibits large cracks with increasing the power density and pulse number under electron beam irradiation and high-intensity pulsed ion beam [25]. It has been reported that thermal shock failure tends to occur in materials with an increasing temperature gradient [26]. Several recent studies have examined the interaction of TTS with the newly developed HEAs. The CoCrFeNiMn HEA coatings with an FCC solid solution and nano-oxides structures exhibited high phase stability and excellent mechanical properties after TTS, with only minor cracks on the surface [27]. More importantly, a fine-grained layer with ~80 μm thickness was generated on the surface of $CrFeCoNiMn_{0.75}Cu_{0.25}$ HEA after laser shock peening treatment with a laser pulse of 18 J, and the microhardness increased significantly [28]. However, the effect of rapid thermal load on reducing the microstructures and performance of activation HEAs remains unexplored. Thus, a fundamental understanding of this phenomenon is critical for the optimization of reduced activation HEAs.

In this work, a reduced activation refractory HEA, $VCrFeTa_{0.2}W_{0.2}$, was synthesized and investigated by TTS tests using electron beams to confirm its microstructure and performance. In addition, the corrosion behavior of the $VCrFeTa_{0.2}W_{0.2}$ HEA was also analyzed and discussed.

2. Experimental details

2.1. Sample preparation

Ingots with a nominal chemical composition of $VCrFeTa_{0.2}W_{0.2}$ (molar ratio) were synthesized by vacuum arc-melting in a Ti-gettered and high-purity argon atmosphere. The metallic elements (V, Cr, Fe, Ta, and W) with a purity of ≥ 99.9 wt% were used because they are reduced activation elements with special properties [29]. The prepared ingots were then cut into small samples with a size of 20 mm (length) × 20 mm (width) × 2 mm (thickness). All the samples were cleaned with alcohol in an ultrasonic bath. The TTS tests were performed using a SEB (M) – 100A vacuum electron beam bombardment furnace (Guilin Strong Numerical 89 Control Vacuum Equipment Co., Ltd., China). During the electron beam bombardment, the chamber pressure of the furnace was kept below 10^{-2} Pa. Additionally, the working voltage and the action time of the beam were set as 30 kV and 200 ms, respectively. The beam spot diameter was 5 mm, and the field frequency was 64 lines. The waveform frequency was set in rectangular 5 K. Two batches of parallel TTS tests were conducted with beam powers of 15 kW and 17 kW and the corresponding experimental parameters were listed in Table 1. The as-cast, reduced activation HEA sample was denoted as S0, while the samples exposed to beam powers of 15 kW and 17 kW were denoted as S1 and S2, respectively.

2.2. Microstructure and properties characterizations

X-ray diffraction (Bruker D8, Karlsruhe, Germany) was conducted to analyze the phase evolution of the alloys using Cu K_α radiation with a tube voltage of 40 kV and a scan speed of 10°/min. The phase composition of each sample was determined by using JADE 6 software. The phase content was analyzed by the whole pattern fitting and Rietveld refinement (WPF Refinement) method. During the calculations, a crystallographic model of each phase was created by the atomic substitution, which was taken from Inorganic Crystal Structure Database (ICSD). The microstructure and morphology were characterized by using a Zeiss Supra55 scanning-electron microscope (SEM). The Vickers microhardness tests were performed by using a load of 200 g and a dwelling time of 15 s. The average value of Vickers microhardness was taken from at least 12 indents for each sample. The electrochemical measurements were tested on a PARSTAT 2273 electrochemical workstation with a standard three-electrode cell system. A saturated calomel electrode (SCE) and a platinum electrode were employed as the reference electrode and auxiliary electrode, respectively. The alloy sample with a size of 5 mm × 5 mm × 2 mm was used as a working electrode, and the corrosion medium consisted of 3.5 wt% NaCl solution. The open circuit potential (OCP) of the sample was held for 10–30 min to achieve a stable voltage. The electrochemical impedance spectroscopy (EIS) experiments were performed at the OCP with a test frequency of 10 mHz~100 KHz. The potentiodynamic-polarization tests were applied to 10^{-2} A/cm^2 with a scan rate of 100 mV/min. The potentiodynamic-polarization experiment was stopped when the current density exceeded 10 mA/cm^2. Both the OCP and potentiodynamic-polarization experiments were performed at least three times to ensure the reproducibility of the results.

Table 1
Electron beam parameters for the $VCrFeTa_{0.2}W_{0.2}$ HEA samples during the TTS.

Samples	Power (kW)	Voltage (kV)	Time (ms)	Field frequency (Hz)	Line frequency (Hz)
S1	15	30	200	64	5000
S2	17	30	200	64	5000

2.3. Refined composite multiscale entropy (RCMSE) technique

The refined composite multiscale entropy (RCMSE) technique was implemented to analyze the dynamical complexity of the current fluctuations. This method has been applied to analyze various phenomena, including the serrated flow in alloys [30–33], chaos [34], and physiological data [35,36]. A higher complexity (sample entropy) value was attributed to "meaningful structural richness" inherent in a data set, while a lower value corresponds to less spatially-correlated behavior. In this work, the RCMSE method was used to analyze the metastable pitting-fluctuation data for samples, S1 and S2, which are represented by the current spikes in the passive region of a given potentiodynamic-polarization curve [37]. A step-by-step guidance relevant to the analysis of metastable pitting data was listed as follows.

(1) The data outside the metastable pitting region are omitted;
(2) The underlying corrosion data trend is eliminated according to the fitting by using a moving average method;
(3) The k_{th} coarse-grained time series are constructed from the detrended data set, and defined as $y^{\tau}_{k,j}$ [38]:

$$y^{\tau}_{k,j} = \frac{1}{\tau}\sum_{i=(j-1)\tau+k}^{j\tau+k-1} x_i; 1 \le j \le \frac{N}{\tau}, 1 \le k \le \tau \quad (1)$$

where x_i is the i_{th} point from the detrended time-series data, τ is the scale factor, N is the total number of data points from the series data, and k is an indexing factor that designates at which data point to initialize analysis.

(4) Vectors with a given y^{τ}_{k} for each τ are created;

$$\boldsymbol{y}^{\tau}_{\boldsymbol{k}} = \left\{ y^{\tau}_{k,1} y^{\tau}_{k,2} \cdots y^{\tau}_{k,M} \right\} \quad (2)$$

where $M = N/\tau$, and each $y^{\tau}_{k,j}$ is determined using Eq. (1).

(5) The template vectors, $y^{\tau,m}_{k,i}$, of dimension m = 2 are created;

$$\boldsymbol{y}^{\tau,m}_{k,i} = \left\{ y^{\tau}_{k,i} y^{\tau}_{k,i+1} \cdots y^{\tau}_{k,i+m-1} \right\}; 1 \le i \le N-m; 1 \le k$$

CORRECTED PROOF

(6) The distance between two template vectors via the infinity norm is measured to determine whether they are matched;

$$d_{jl}^{\tau,m} = \left\| \boldsymbol{y}_j^{\tau,\boldsymbol{m}} - \boldsymbol{y}_l^{\tau,\boldsymbol{m}} \right\|_\infty = \max\left\{ \left| y_{1,j}^{\tau} - y_{1,l}^{\tau} \right| \cdots \left| y_{i+m-1,j}^{\tau} - y_{i+m-1,l}^{\tau} \right| \right\} <$$

where r is a predefined tolerance value, which is typically 0.15 times of the standard deviation of the data [39–41]. Two vectors are considered as a match if $d_{jl}^{\tau,m}$ is less than r.

(7) Steps (1) - (4) are repeated for m = m + 1.

(8) The RCMSE value is calculated and denoted as the sample entropy for this investigation. The first sum of the number of matching pairs are used, $n_{k,\tau}^{m}$ and $n_{k,\tau}^{m+1}$, for k from 1 to τ and the solved by using the following equation [38]:

$$RCMSE(\boldsymbol{X}, \quad \tau, \quad m, \quad r) = Ln\left(\frac{\sum_{k=1}^{\tau} n_{k,\tau}^{m}}{\sum_{k=1}^{\tau} n_{k,\tau}^{m+1}} \right) \tag{5}$$

3. Results and discussion

The X-ray diffraction patterns of S0, S1, and S2 are shown in Fig. 1. It can be seen that the S0 sample consisted of two body-centered-cubic (BCC) phases as well as a Laves phase. After TTS, the characteristic peaks of the Laves phase in S1 and S2 samples were more pronounced than that of S0. Besides, the main peak near 43.5° of S1 and S2 was significantly broadened, indicating that the grains of the BCC1 phase in S1 and S2 was significantly refined after TTS. The Debye-Scherrer [42,43] formula was used to estimate the grain size.

$$D = K\lambda / (\beta\cos\theta) \tag{6}$$

where D is the grain size; K is a constant related to the definition of β and 0.89 in this work; β is the line broadening at half the maximum intensity; λ is the X-ray wavelength (copper K_α, λ = 0.154056 nm); θ is the diffraction angle.

It can be calculated that the grain sizes of S0, S1 and S2 are 168 nm, 106 nm, and 97 nm, respectively. In addition, the peak positions of the BCC1 phase in S1 and S2 have shifted slightly to higher angles. According to the Bragg equation[44,45], the lattice constants of the BCC1 phase in S0, S1, and S2 were calculated to be 0.2937 nm, 0.2925 nm, and 0.2920 nm, respectively. Therefore, after TTS, the $VCrFeTa_{0.2}W_{0.2}$ HEAs exhibited greater changes in the phase structures, grain sizes and lattice constants.

SEM equipped with EDS was applied to determine the phase microstructure and chemical composition of S0, S1, and S2. Fig. 2 presents the SEM images of the $VCrFeTa_{0.2}W_{0.2}$ HEAs. The S0 displayed a clear dendrite structure, as shown in Fig. 2**(a1).** The white region in Fig. 2 **(a2)** indicated a Laves phase with the inter-dendritic structure, while the gray and black regions were composed of the BCC1 and BCC2 phases with dendritic structure, respectively. The chemical composi-

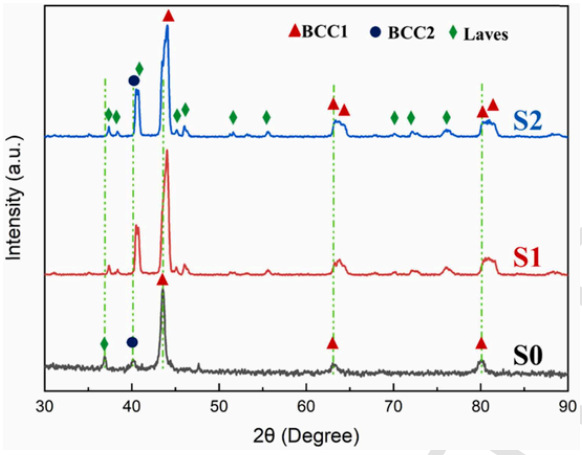

Fig. 1. XRD patterns of the reduced activation $VCrFeTa_{0.2}W_{0.2}$ HEAs.

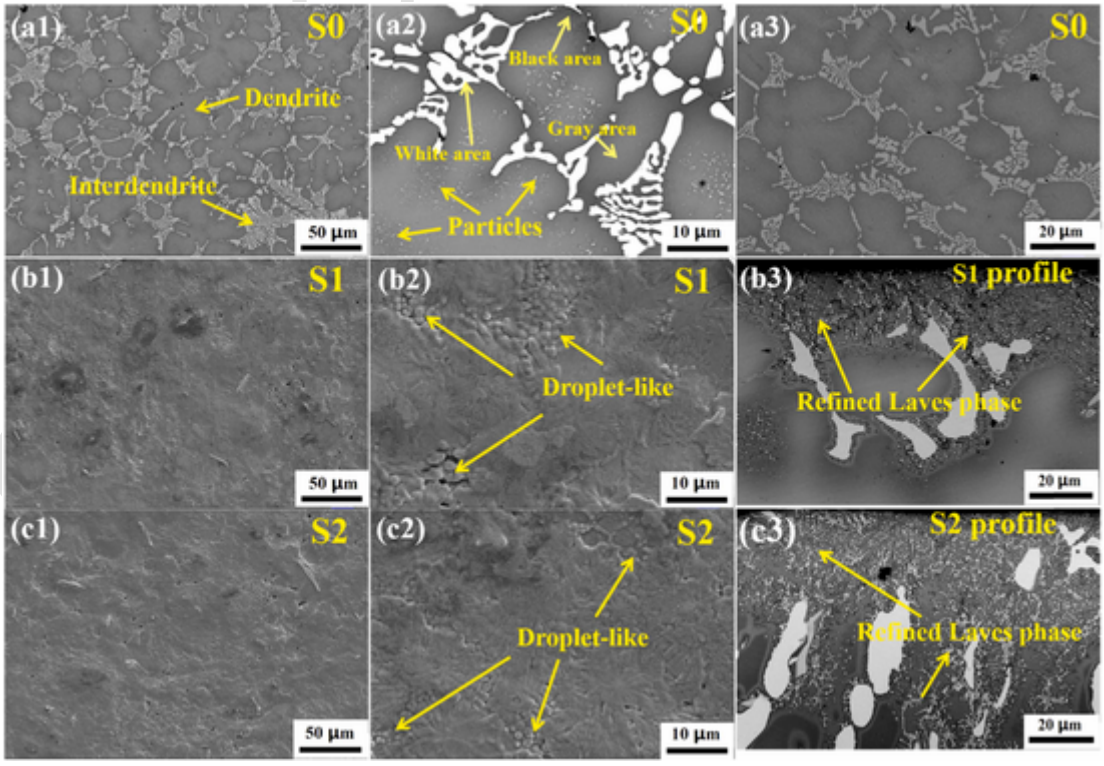

Fig. 2. SEM surface images of samples S0, S2 and S2.

tions of the different regions are listed in Table 2. It can be seen that the black region was rich in V and Fe. The gray region mainly consisted of V, Cr, and W. The white region was mainly composed of Fe and Ta. In addition, the nanoscale white Laves particles Fe_2Ta were randomly distributed in the dendritic matrix. Fig. 2**(b-c)** show the SEM surface images of S1 and S2. No obvious difference was observed from these figures, indicating that the alloy surface melted and solidified rapidly after TTS to achieve a homogenous surface layer having uniform alloy composition. A droplet-like solidification structure was distributed around snowflake-like dendrites due to the rapid temperature drop after TTS. The S2 alloy exhibited a finer microstructure and a smaller droplet-like structure than the S1 alloy, suggesting that an increase in the TTS power promoted the melting of the surface and enhanced the fluidity. In addition, a higher solidification rate resulted in a finer surface morphology. Fig. 2**(b3-c3)** present the cross-sectional backscatter diagrams for S1 and S2. It can be seen that the remelted layer had a thickness of ~50 μm at 15 kW and 60 μm at 17 kW. Compared with Fig. 2**(a3)**, the Laves phase was greatly refined after TTS with a higher content than that in the as-cast alloy. As listed in Table 3, the content of BCC1 phase decreased significantly after TTS, while those of BCC2 and Laves phases increased.

Table 2
Chemical compositions in different regions of S0 analyzed by EDS (atomic percentage, at%).

Region	V	Cr	Fe	Ta	W
Overall	31.15 ± 0.21	29.97 ± 0.31	28.58 ± 0.40	5.01 ± 0.59	5.29 ± 0.08
White	15.98 ± 0.18	23.30 ± 0.21	38.75 ± 0.32	21.96 ± 0.49	/
Gray	35.57 ± 0.21	33.72 ± 0.19	21.95 ± 0.21	2.76 ± 0.31	6 ± 0.07
Black	32.41 ± 0.18	26.72 ± 0.16	39.49 ± 0.24	1.39 ± 0.11	/

Table 3
The contents (wt%) of BCC1, BCC2 and Laves phases in S0, S1, and S2 alloys.

Samples	S0	S1	S2
Phase			
BCC1	94.5	73.6	72.8
BCC2	2.4	5.4	5.5
Laves	3.1	21.0	21.7

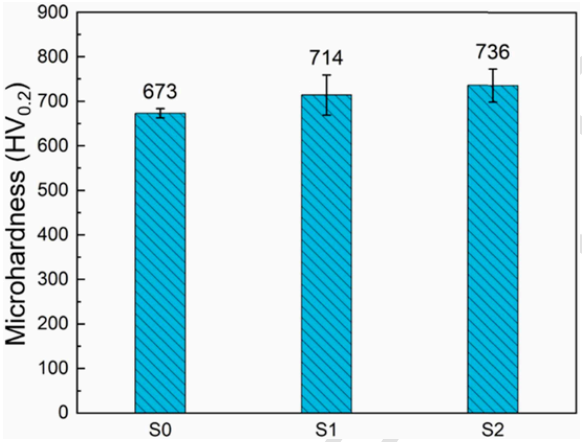

Fig. 3. Microhardness of samples S0, S1 and S2.

As shown in Fig. 3**,** the microhardness of S0, S1, and S2 were ~673 HV, ~714 HV and ~736 HV, respectively. The significant enhancement of the microhardness of reduced activation HEA after the TTS could be attributed to the grain refinement of the surface layer. The increased microhardness was consistent with the increase in the Laves phase content at a higher electron-beam power.

Fig. 4**(a)** shows the polarization plots of S0, S1 and S2 that were exposed to 3.5 wt% NaCl solution. The fitted corrosion current density (I_{corr}) and self-corrosion potential (E_{corr}) data are listed in Table 4. The E_{corr} represents the potential of materials in an OCP and the I_{corr} is used to calculate the corrosion rate of the material. Generally, I_{corr} is mainly applied to evaluate the corrosion resistance of samples, followed by E_{corr} and the passivation range [46,47].

As shown in Fig. 4(a), S1 and S2 exhibited unique metastable and serration corrosion behaviors in NaCl solution, which were completely different with the as-cast one. At the beginning of the anodic-polarization curve, the corrosion current density of the samples exhibited a rapid upward tendency with an increase in scanning voltage, indicating that the samples possessed an active dissolution process in the initial stage of corrosion. As the scanning voltage increased, all samples demonstrated passivation behaviors, and formed a protective passiva-

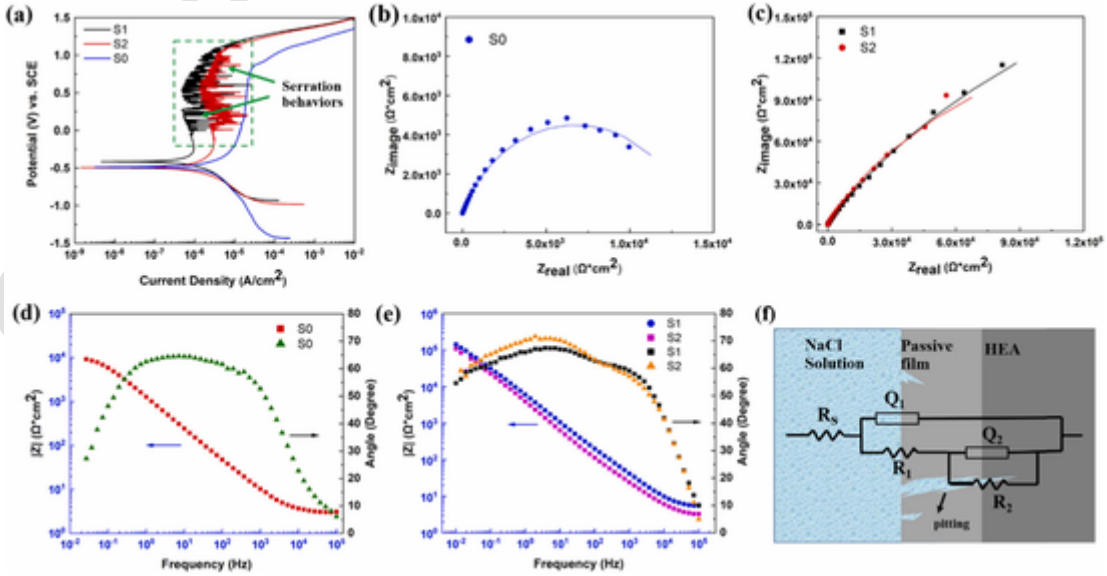

Fig. 4. (a) Potentiodynamic-polarization plots; (b) and (c) Nyquist plots; (d) and (e) Bode plots; (f) equivalent circuit for the HEAs of the electrochemical impedance spectroscopy (EIS) in 3.5 wt% NaCl solution at room temperature.

Table 4
Electrochemical parameters and equivalent circuit parameters for EIS of samples S0, S1, and S2 with different processes in 3.5 wt% NaCl solution.

Alloys	E_{corr} (V_{SCE})	I_{corr} (μA/cm^2)	E_{pit} (V_{SCE})	R_S (Ω cm^2)	R_1 (Ω cm^2)	R_2 (Ω cm^2)	Q_1		Q_2	
							Y_0 (F/cm^2)	n	Y_0 (F/cm^2)	n
S0	- 0.483	1.361	0.881	2.84	262.8	1.32×10^4	1.44×10^{-4}	0.76	4.57×10^{-5}	0.71
S1	- 0.411	0.472	1.165	5.06	101.3	6.71×10^5	1.45×10^{-5}	0.83	3.01×10^{-5}	0.77
S2	- 0.494	0.547	1.112	3.14	41.7	4.17×10^5	1.80×10^{-5}	0.86	4.51×10^{-5}	0.73

tion film to prevent the further corrosion and dissolution. The small corrosion potential represented a low chemical stability, and a high corrosion tendency of materials in the corrosion solution [48,49]. It could be observed that the E_{pit} (pitting potential) was improved after the surface treatment from 0.881 V_{SCE} in the as-cast condition to 1.165 V_{SCE} and 1.112 V_{SCE} in S1 and S2, respectively. The I_{corr} values of S1 and S2 in 3.5 wt% NaCl solution were 0.472 μA/cm^2 and 0.547 μA/cm^2, respectively, much smaller than that of S0, indicating that the corrosion resistance of the HEAs was significantly improved after TTS.

During the electrochemical reaction, the passivation film has a protective effect and could effectively reduce the current density during the corrosion process, and improve the corrosion resistance [48,50]. Fig. 4(b-e) display the Nyquist and Bode plots of S0, S1 and S2 in 3.5 wt% NaCl solution for OCP. The Nyquist curves are all semicircular arcs with a concave center below the X-axis. The radius of the impedance indicates the quality of corrosion resistance, in which a larger arc radius corresponds to a higher corrosion resistance [49,50]. It can be seen that the Nyquist curve of S1 presents the largest arc radius, followed by those of S2 and S0, indicating the corrosion resistance of these alloys followed the order of S1 > S2 > S0.

The Bode plots of S0, S1, and S2 suggested that the resistance value of S0 is one order of magnitude lower than those of S1 and S2, and the resistance value of S1 is slightly larger than S2. Meanwhile, the stable phase angles in a range of 60 ~ 70° and inclined impedance-modulus values appear at low and medium frequencies, which indicated the presence of a barrier oxide film on the surface was expected to have a capacitive response. Based on the shape of the Bode plots, S1 and S2 has a quadratic constant, while S0 has a first-order constant, which could be ascribed to the elemental segregation, structural inhomogeneity and surface defects of the as-cast samples. The equivalent circuit diagram in Fig. 4(f) shows the best fitting results of experimental data. The first part was related with a surface covered with a complete passivation film, and the circuit was composed of a solution resistance R_S, and a passivation film capacitor Q_1. The second part was applied to characterize the charge-transfer process in the weak and sensitive areas of the passivation film, in which the circuit consisted of a solution resistance R_1 in the weakened area, the charge transfer resistance R_2, and the capacitance Q_2 in the weakened area.

Table 4 lists the fitted parameters of the EIS. The Y_0 is the scale factor of the capacitance impedance, and inversely proportional to the capacitance impedance. The n refers to the dispersion degree of the capacitance [50,51]. After TTS, the Y_0 value of the $VCrFeTa_{0.2}W_{0.2}$ HEA decreased, while the n in Q_1 increased, indicating that a more protective passivation film with a reduced porosity was formed on the surface [49]. The charge-transfer resistance R_2 in the weak region of the passivation film increased from 1.32×10^4 Ω cm^2 in the as-cast state to 6.71×10^5 Ω cm^2 in S1 and 4.17×10^5 Ω cm^2 in S2. At the same time, the sensitive and weak area of the passivation film, the S1 presented the largest polarization resistance (R_p, $R_p = R_1 + R_2$), while the S0 displayed the smallest. The higher the charge transfer resistance, the more difficult it is for ions to transfer through the capacitor. Thus, the corrosion performance of the alloys followed in the order of S1 > S2 > S0. The results of the EIS were consistent with the potentiodynamic-polarization experiments.

The dissolution morphologies of S0, S1 and S2 after the polarization tests are shown in Fig. 5. As exhibited in Fig. 5(a), the dendrite edge displayed a rough V-rich region in the S0 alloy after the polarization test. The inset image revealed that the Laves phase between the dendrites maintains morphological features due to the V-rich region being attacked by Cl^- ions that typically occurred during localized corrosion. These results indicated that the Laves phase possessed a higher corrosion resistance than the BCC phases, and S0 exhibited phase boundary corrosion. It can be seen from the corrosion morphologies of S1 and S2 alloys shown in Fig. 5(b-c) that only a few hemispherical pits were distributed on the surfaces. The treated surface layer had network-shaped Laves phase, which endowed the BCC solid-solution phases with a highly-protective layer, and thus improved the corrosion resistance of the alloy. According to the features in Fig. 5(b-c), it can be observed that the number of corrosion pits on the alloy surface increased with increasing the power of the TTS. In addition, the reduced corrosion resistance was consistent with the results of the polarization tests.

The corrosion resistance of the alloy was improved after TTS. The E_{pit} of the $VCrFeTa_{0.2}W_{0.2}$ alloy was determined to be 1.165 V_{SCE} at 15 kW and 1.112 V_{SCE} at 17 kW, which exceeded that of stainless steels in 3.5 wt% NaCl solution. Fig. 6 compares the E_{pit} and I_{corr} of this work with conventional corrosion-resistant alloys [48,52] and some reported HEAs [49,51–60]. Most HEAs exhibited higher E_{pit} values than conventional corrosion-resistant alloys [48,49,52], such as stainless steels, Ni-alloys, and Ti-alloys. In particular, the HEAs with a BCC structure exhibited both low I_{corr} and high E_{pit} values, suggesting that this type of HEA was capable for applications in the fields of seawater desalination, naval weapons and chemical vessels. As for the $VCrFeTa_{0.2}W_{0.2}$ HEA after TTS by the electron beam, the E_{pit} value was even higher than the reported FCC and FCC + BCC dual-phase HEAs, as well as most BCC HEAs. This feature indicated the TTS strategy has potential application prospects in improving the corrosion resistance of materials.

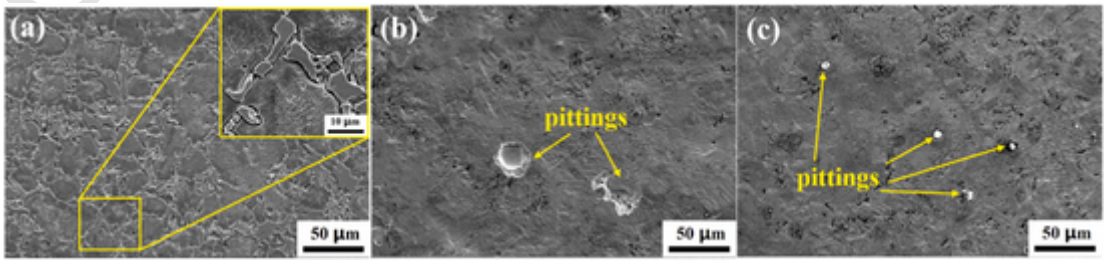

Fig. 5. SEM surface images of the $VCrFeTa_{0.2}W_{0.2}$ HEAs after potentiodynamic polarization in 3.5 wt% NaCl solution. (a) S0, (b) S1, and (c) S2.

CORRECTED PROOF

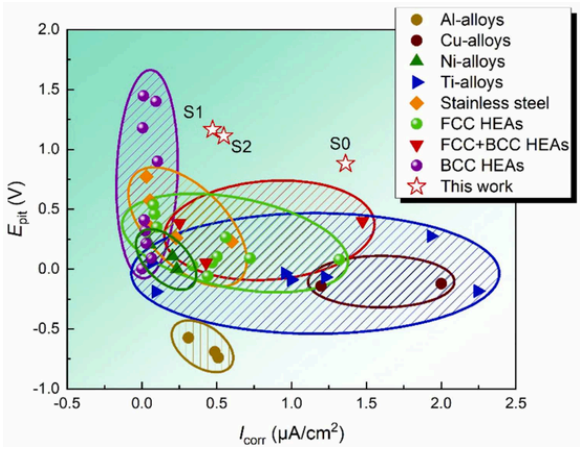

Fig. 6. Comparison of E_{pit} and I_{corr} values for the $VCrFeTa_{0.2}W_{0.2}$ HEAs, conventional corrosion-resistant alloys, and some reported HEAs in the 3.5 wt% NaCl solution.

Fig. 7(a) shows the RCMSE analysis results for S1 and S2 with scale factors ranging from 1 to 20. Both curves were found to increase with increasing the scale factor, suggesting a complex behavior of current fluctuations [61]. Furthermore, the curve for S1 was higher than that for S2 when the scale factors were above 10. A larger sample-entropy value indicated that the fluctuations of S1 contained more complex behavior than those for S2. Conversely, the fluctuations in S2 exhibited a lower sample-entropy value, indicating a less spatially correlation and more random behavior.

The sample-entropy curves over a given range of scale factors were integrated to quantitatively analyze and compare the results of Fig. 7(a). The corresponding area under the curve was denoted as A_{SE}, and a higher value corresponded to a more complex current fluctuations [62]. It was found that these values were 24.89 and 24.12 for S1 and S2, respectively. After comparing with the results of Table 3, there was a positive correlation between A_{SE} and R_p values, indicating that the samples with more complex behavior of metastable pitting-current fluctuations exhibited a greater corrosion resistance.

Statistical analysis was performed on the metastable pitting current fluctuations for the surface-modified samples. The complementary cumulative distribution function (CCDF) was calculated via the following equation.

$$C(S) = \int_S^{\infty} D(S')\, dS' \tag{7}$$

where C(S) is the integral of the probability distribution function of the current fluctuations, S, from S to infinity. For the current investigation, a current fluctuation magnitude of 0.2 μA/cm^2 was employed as the noise threshold [49]. Fig. 7(b) features the distribution of S1 and S2. It can be seen that the electron beam energy was significantly dependent on the current fluctuation amplitude. Specifically, the increase in beam energy greatly increased the likelihood of great current fluctuations during metastable pitting. Furthermore, S1 with a smaller distribution of current fluctuations was more resistant to corrosion, suggesting that the corrosion resistance and the complexity of current fluctuations were inversely related to the magnitude of current fluctuations during metastable pitting.

Compared with S2, a higher complexity value of S1 corresponded to a greater corrosion resistance and current-fluctuation distribution with a lower magnitude of current fluctuations. The relation between complexity and corrosion resistance of the sample could be explained as follows. The S2 displayed a rougher surface than S1, representing its more random surface topology [63]. Consequently, the more random surface profile would result in a lower spatial correlation of anodic reactions during metastable pitting, and thus a less dynamically complex. Conversely, the current spikes on smooth surface would exhibit a higher degree of spatial correlation and more complex behavior. In terms of the statistical analysis, the current spike of S1 has a smaller magnitude for SI, as shown in Fig. 7(b), indicating a reduced probability of the nucleated metastable pit propagation and hence a higher corrosion resistance [64].

4. Summary

In this work, the effects of TTS on the microstructures and corrosion properties of the reduced activation $VCrFeTa_{0.2}W_{0.2}$ HEAs were investigated. It was found that the as-cast $VCrFeTa_{0.2}W_{0.2}$ HEAs were consisted of BCC1, BCC2 phases as well as a Laves phase. After the TTS treatment, the Laves phases content increased, while the BCC1 phase content reduced greatly. The grain size was refined and the microhardness was enhanced from ~673 HV to ~714 HV. After the TTS treatment, the corrosion resistance of this alloy was improved with a low corrosion current density of ~0.472 μA/cm^2 in 3.5 wt% NaCl solution. A new pitting-current serration behavior was observed in the passivation area, as determined by the potentiodynamic polarization curves. Dynamical and statistical analyses of the metastable pitting-current fluctuations revealed that the corrosion resistance was related to current-fluctuation distributions with a lower overall spike magnitude and a higher dynamical complexity.

The reduced activation $VCrFeTa_{0.2}W_{0.2}$ HEA after TTS treatment exhibited outstanding mechanical properties and corrosion resistance. Therefore, the TTS could be performed as an efficient surface modification technique to improve the mechanical properties of HEAs. Although the modification is limited by the penetration depth of the electron beams, these issues could be addressed by increasing the energy density

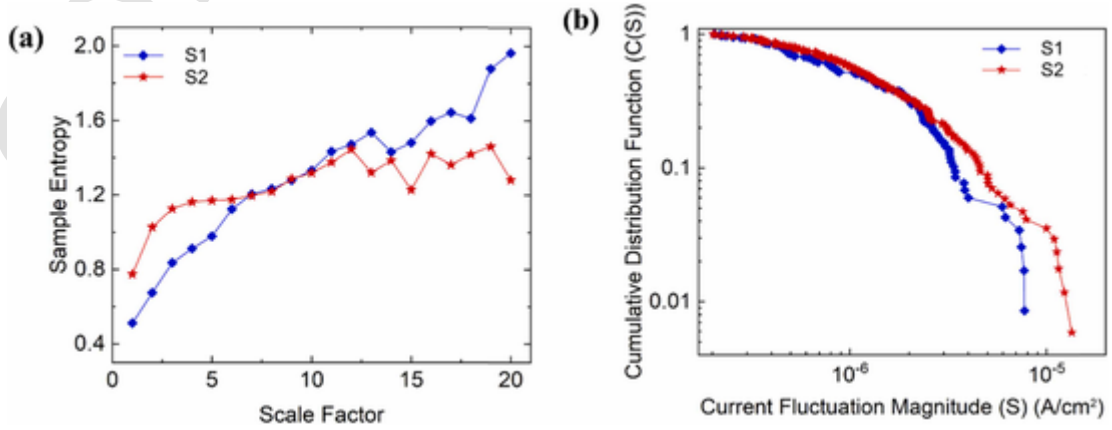

Fig. 7. (a) Sample entropy vs. scale factor for S1 and S2; (b) CCDFs for the metastable pitting-current fluctuations for S1 and S2.

CORRECTED PROOF

and treatment time. Therefore, the TTS treatment opened up new opportunity to functionalize HEA materials with better performance.

CRediT authorship contribution statement

W.R. Z. carried out the experiments; W.R. Z., W.B. L., J.L. R., and J. B. analyzed the data; W.R. Z. and W.B. L. wrote the drafts. Y. Z. and W.B. L. offered the theoretical guidance. All authors contributed to the discussion, review & editing.

Declaration of Competing Interest

The authors declare that they have no known competing financial interests or personal relationships that could have appeared to influence the work reported in this paper.

Acknowledgments

This research was supported from the Xi 'an Postdoctoral Innovation Base Project, Fundamental Research Funds for the Central Universities (Grant No. FRF-MP-18-003/ FRF-MP-19-013), Key Research and Development Program of Shaanxi (No. 2021GY-249), Innovation Center of Nuclear Materials for National Defense Industry (ICNM-2021-ZH-16). W.B.L. would like to thank the National Natural Science Foundation of China (Grant No. 51801128), Guangdong Basic and Applied Basic Research Foundation (Grant Nos. 2021A1515012278 and 2022A1515010288). J.L.R. would like to thank the National Natural Science Foundation of China (Grant No. 52071298). P.K.L. very much appreciates the supports of (1) the U.S. Army Research Office Project (W911NF-13-1-0438 and W911NF-19-2-0049) with the program managers, Drs. M. P. Bakas, S. N. Mathaudhu, and D. M. Stepp and (2) the National Science Foundation (DMR-1611180 and 1809640) with the program directors, Drs. J. Yang, G. Shiflet, and D. Farkas.

References

[1] D.B. Miracle, High entropy alloys as a bold step forward in alloy development, Nat. Commun. 10 (2019) 1805.
[2] W.R. Zhang, P.K. Liaw, Y. Zhang, Science and technology in high-entropy alloys, Sci. China Mater. (2018) 1–21.
[3] C. Zlotea, M.A. Sow, G. Ek, J.P. Couzinié, L. Perrière, I. Guillot, J. Bourgon, K.T. Møller, T.R. Jensen, E. Akiba, M. Sahlberg, Hydrogen sorption in TiZrNbHfTa high entropy alloy, J. Alloy. Compd. 775 (2019) 667–674.
[4] D.X. Qiao, H. Liang, S.Y. Wu, J.Y. He, Z.Q. Cao, Y.P. Lu, T.J. Li, The mechanical and oxidation properties of novel B2-ordered $Ti_2ZrHf_{0.5}VNb_{0.5}Al_x$ refractory high-entropy alloys, Mater. Charact. 178 (2021) 111287.
[5] Y.K. Mu, L.H. He, S.H. Deng, Y.F. Jia, Y.D. Jia, G. Wang, Q.J. Zhai, P.K. Liaw, C.T. Liu, A high-entropy alloy with dislocation-precipitate skeleton for ultrastrength and ductility, Acta Mater. 232 (2022) 117975.
[6] T.N. Yang, C.Y. Lu, G. Velisa, K. Jin, P.Y. Xiu, Y.W. Zhang, H.B. Bei, L.M. Wang, Influence of irradiation temperature on void swelling in NiCoFeCrMn and NiCoFeCrPd, Scr. Mater. 158 (2019) 57–61.
[7] Y.P. Lu, H. Huang, X.F. Gao, C.L. Ren, J. Gao, H.Z. Zhang, S.J. Zheng, Q.Q. Jin, Y.H. Zhao, C.Y. Lu, T.M. Wang, T.J. Li, A promising new class of irradiation tolerant materials: $Ti_2ZrHfV_{0.5}Mo_{0.2}$ high-entropy alloy, Mater. Sci. Technol. 35 (2019) 369–373.
[8] M. Sadeghilaridjani, A. Ayyagari, S. Muskeri, V. Hasannaeimi, R. Salloom, W.Y. Chen, S. Mukherjee, Ion irradiation response and mechanical behavior of reduced activity high entropy alloy, J. Nucl. Mater. 529 (2020) 151955.
[9] L.X. Yang, H.L. Ge, J. Zhang, T. Xiong, Q.Q. Jin, Y.T. Zhou, X.H. Shao, B. Zhang, Z.W. Zhu, S.J. Zheng, X.L. Ma, High He-ion irradiation resistance of CrMnFeCoNi high-entropy alloy revealed by comparison study with Ni and 304SS, J. Mater. Sci. Technol. 35 (2019) 300–305.
[10] O. El-Atwani, N. Li, M. Li, A. Devaraj, J.K.S. Baldwin, M.M. Schneider, D. Sobieraj, J.S. Wróbel, D. Nguyen-Manh, S.A. Maloy, E. Martinez, Outstanding radiation resistance of tungsten-based high-entropy alloys, Sci. Adv. 5 (2019) eaav2002.
[11] T. Cheng, W.J. Qin, Y.Y. Lian, X. Liu, J. Tang, G.X. Cai, S.J. Zhan, X.Y. Le, C.Z. Jiang, F. Ren, High transient-thermal-shock resistant nanochannel tungsten films, Nanomaterials 11 (2021).
[12] Y. Ueda, K. Schmid, M. Balden, J. Coenen, T. Loewenhoff, A. Ito, A. Hasegawa, C. Hardie, M. Porton, M. Gilbert, Baseline high heat flux and plasma facing materials for fusion, Nucl. Fusion 57 (2017) 092006.
[13] M. Chen, H.J. Wang, H.Y. Jin, X.D. Pan, Z.H. Jin, Transient thermal shock behavior simulation of porous silicon nitride ceramics, Ceram. Int. (2016).
[14] M. Gago, A. Kreter, B. Unterberg, M. Wirtz, Synergistic and separate effects of plasma and transient heat loads on the microstructure and physical properties of ITER-grade tungsten, Phys. Scr. 96 (2021) 124052.
[15] Leonid N. Vyacheslavov, Alexander A. Vasilyev, Alexey S. Arakcheev, D.E. Cherepanov, Igor V. Kandaurov, Alexander A. Kasatov, Vladimir A. Popov, Alexey A. Ruktuev, Alexander V. Burdakov, Galina G. Lazareva, Anastasia G. Maksimova, Andrey A. Shoshin, In-situ study of the processes of damage to the tungsten surface under transient heat loads possible in ITER, J. Nucl. Mater. 544 (2021) 152669.
[16] S.M. Wang, J.S. Li, Y. Wang, X.F. Zhang, R.P. Wang, Y.R. Wang, J. Cao, Thermal damage of tungsten-armored plasma-facing components under high heat flux loads, Sci. Rep. 10 (2020) 1359.
[17] Y. Wang, W. Guo, Y. Zhu, Y. Yuan, J. Peng, M. Ren, Z. Wang, L. Cheng, Z. Chen, Y. Lian, X. Liu, G.H. Lu, Effect of helium pre-implantation on the thermal shock performance of tungsten, Nucl. Mater. Energy 27 (2021) 100934.
[18] M.M. Wang, Z.M. Xie, H.W. Deng, R. Liu, J.F. Yang, T. Zhang, X.P. Wang, Q.F. Fang, C.S. Liu, X. Liu, Y. Xiong, Thermal shock fatigue behaviors of various W-0.5 wt%ZrC materials under repetitive transient heat loads, J. Nucl. Mater. 534 (2020) 152152.
[19] X. Zan, J. Yan, H.T. Sun, K. Wang, Y.Y. Lian, X.Y. Tan, L.M. Luo, X. Liu, Y.C. Wu, Surface damage during transient thermal load of 50% thickness reduced W-2% (Vol.) Y_2O_3 sheet with different recrystallization volume fraction, Int. J. Refract. Met. Hard Mater, 88 (2020) 105197.
[20] M. Wirtz, J. Linke, T. Loewenhoff, G. Pintsuk, I. Uytdenhouwen, Transient heat load challenges for plasma-facing materials during long-term operation, Nucl. Mater. Energy (2016) 148–155.
[21] Y.Y. Chen, H.X. Hou, G. Yao, D.G. Liu, L.M. Luo, C. Li, C.X. Liu, Y. Huang, Z.M. Wang, Transient thermal shock and helium ion irradiation damage behaviors of ODS-W/CuCrZr joints, Mater. Charact. 184 (2022) 111710.
[22] W. Nelson, A. Chemey, M. Hertz, E. Choi, D. Graf, S. Latturner, T. Albrecht-Schmitt, K. Wei, R. Baumbach, Superconductivity in a uranium containing high entropy alloy, Sci. Rep. 10 (2020) 1–8.
[23] X.L. Wang, M.J. He, Z.X. Guo, F. Wang, D.L. Zhou, Z.X. Wu, J.J. Huang, Preliminary studies on the main characteristics and transient heat shock performances of detonation sprayed tungsten coatings on 316 L steel substrates, Surf. Coat. Technol. 429 (2022) 127946.
[24] H.Y. Chen, L.M. Luo, X. Zan, Q. Xu, K. Tokunaga, J.Q. Liu, D.G. Liu, X.Y. Zhu, J.G. Cheng, Y.C. Wu, Transient thermal shock behavior of W–Zr/Sc_2O_3 composites prepared via spark plasma sintering, Fusion Eng. Des. 126 (2018) 44–50.
[25] H.A. Bo, H.A. Bo, X.A. Ye, B. Yl, L.B. Xiang, A. Jt, Preparation and thermal shock characterization of yttrium doped tungsten-potassium alloy, J. Alloy. Compd. 686 (2016) 298–305.
[26] X.Y. Fan, H.J. Wang, M. Niu, D.D. Zhang, J. Zhou, J.P. Fan, Experiments and transient finite element simulation of γ-Y_2 Si_2O_7 / B_2O_3 -Al_2O_3-SiO_2 glass coating on porous Si_3N_4 substrate under thermal shock, Ceram. Int. (2017) S0272884217326743.
[27] J.T. Liu, S.W. Liu, H.L. Zheng, W.J. Huang, W. Zhao, W.B. Liao, Effects of transient thermal shock on the microstructure and mechanical properties of CoCrFeNiMn high-entropy alloy coatings, Front. Mater. 8 (2021).
[28] W.J. Fu, Y.J. Huang, J.F. Sun, A.H.W. Ngan, Strengthening $CrFeCoNiMn_{0.75}Cu_{0.25}$ high entropy alloy via laser shock peening, Int. J. Plast. 154 (2022) 103296.
[29] W.R. Zhang, K.P. Liaw, Y. Zhang, A. Novel, Low-Activation $VCrFeTa_xW_x$ (x = 0.1, 0.2, 0.3, 0.4, and 1) high-entropy alloys with excellent heat-softening resistance, Entropy 20 (2018).
[30] J. Brechtl, B.L. Chen, X. Xie, Y. Ren, J.D. Venable, P.K. Liaw, S.J. Zinkle, Entropy modeling on serrated flows in carburized steels, Mater. Sci. Eng. A. 753 (2019) 135–145.
[31] J. Brechtl, X. Xie, Z. Wang, J.W. Qiao, P.K. Liaw, Complexity analysis of serrated flows in a bulk metallic glass under constrained and unconstrained conditions, Mater. Sci. Eng. A. 771 (2020) 138585.
[32] B. Zhang, P.K. Liaw, J. Brechtl, J. Ren, X. Guo, Y. Zhang, Effects of Cu and Zn on microstructures and mechanical behavior of the medium-entropy aluminum alloy, J. Alloy. Compd. 820 (2020) 153092.
[33] J. Moon, E. Tabachnikova, S. Shumilin, T. Hryhorova, Y. Estrin, J. Brechtl, P.K. Liaw, W. Wang, K.A. Dahmen, H.S. Kim, Unraveling the discontinuous plastic flow of a Co-Cr-Fe-Ni-Mo multiprincipal-element alloy at deep cryogenic temperatures, Phys. Rev. Mater. 5 (2021) 083601.
[34] J. Brechtl, X. Xie, P.K. Liaw, S.J. Zinkle, Complexity modeling and analysis of chaos and other fluctuating phenomena, Chaos Soliton Fract. 116 (2018) 166–175.
[35] E. Blons, L.M. Arsac, P. Gilfriche, V. Deschodt-Arsac, Multiscale entropy of cardiac and postural control reflects a flexible adaptation to a cognitive task, Entropy 21 (2019) 13.
[36] J. Escudero, E. Acar, A. Fernandez, R. Bro, Multiscale entropy analysis of resting-state magnetoencephalogram with tensor factorisations in Alzheimer's disease, Brain Res. Bull. 119 (2015) 136–144.
[37] Y.M. Tang, Y. Zuo, J.N. Wang, X.H. Zhao, B. Niu, B. Lin, The metastable pitting potential and its relation to the pitting potential for four materials in chloride solutions, Corros. Sci. 80 (2014) 111–119.
[38] S.D. Wu, C.W. Wu, S.G. Lin, K.Y. Lee, C.K. Peng, Analysis of complex time series using refined composite multiscale entropy, Phys. Lett. A 378 (2014) 1369–1374.
[39] M.D. Costa, A.L. Goldberger, Generalized multiscale entropy analysis:application to quantifying the complex volatility of human heartbeat time series, Entropy 17 (2015) 1197–1203.
[40] M. Costa, A.L. Goldberger, C.K. Peng, Multiscale entropy analysis of biological signals, Phys. Rev. E 71 (2005) 021906.
[41] M. Costa, A.L. Goldberger, C.K. Peng, Multiscale entropy analysis of complex physiologic time series, Phys. Rev. Lett. 89 (2002) 068102.

CORRECTED PROOF

[42] W.M. Guo, B. Liu, Y. Liu, T.C. Li, A. Fu, Q.H. Fang, Y. Nie, Microstructures and mechanical properties of ductile NbTaTiV refractory high entropy alloy prepared by powder metallurgy, J. Alloy. Compd. 776 (2019) 428–436.
[43] Y. Xu, G.D. Li, G. Li, F.Y. Gao, Y. Xia, Effect of bias voltage on the growth of super-hard (AlCrTiVZr)N high-entropy alloy nitride films synthesized by high power impulse magnetron sputtering, Appl. Surf. Sci. 564 (2021) 150417.
[44] Q.K. Shen, X.D. Kong, X.Z. Chen, X.K. Yao, V.B. Deev, E.S. Prusov, Powder plasma arc additive manufactured CoCrFeNi(SiC)x high-entropy alloys: microstructure and mechanical properties, Mater. Lett. 282 (2021) 128736.
[45] R. Li, Y.M. Ma, X.S. Liu, Y. Lu, Y.F. Zhang, P.F. Yu, G. Li, Effect of defects on the phase transition of $Al_{0.1}$CoCrFeNi high-entropy alloy under high pressure, Intermetallics 140 (2022) 107388.
[46] S.Y. Chen, Z.B. Cai, Z.X. Lu, J.B. Pu, R. Chen, S.J. Zheng, C.L. Mao, S.J. Chen, Tribo-corrosion behavior of VAlTiCrCu high-entropy alloy film, Mater. Charact. 157 (2019) 109887.
[47] T.W. Lu, C.S. Feng, Z. Wang, K.W. Liao, Z.Y. Liu, Y.Z. Xie, J.G. Hu, W.B. Liao, Microstructures and mechanical properties of $CoCrFeNiAl_{0.3}$ high-entropy alloy thin films by pulsed laser deposition, Appl. Surf. Sci. 494 (2019) 72–79.
[48] Q.Y. Zhou, S. Sheikh, P. Ou, D.C. Chen, Q. Hu, S. Guo, Corrosion behavior of $Hf_{0.5}Nb_{0.5}Ta_{0.5}Ti_{1.5}Zr$ refractory high-entropy in aqueous chloride solutions, Electrochem. Commun. 98 (2019) 63–68.
[49] Y.Z. Shi, B. Yang, X. Xie, J. Brechtl, K.A. Dahmen, P.K. Liaw, Corrosion of Al_xCoCrFeNi high-entropy alloys: Al-content and potential scan-rate dependent pitting behavior, Corros. Sci. 119 (2017) 33–45.
[50] D.H. Xiao, P.F. Zhou, W.Q. Wu, H.Y. Diao, M.C. Gao, M. Song, P.K. Liaw, Microstructure, mechanical and corrosion behaviors of AlCoCuFeNi-(Cr,Ti) high entropy alloys, Mater. Des. 116 (2017) 438–447.
[51] L. Wei, Y. Liu, Q. Li, Y.F. Cheng, Effect of roughness on general corrosion and pitting of $(FeCoCrNi)_{0.89}(WC)_{0.11}$ high-entropy alloy composite in 3.5 wt% NaCl solution, Corros. Sci. 146 (2019) 44–57.
[52] Y.Z. Shi, B. Yang, P.K. Liaw, Corrosion-resistant high-entropy alloys: a review, Metals 7 (2017) 43.
[53] Z.D. Han, N. Chen, S.Y. Lu, H.W. Luan, R.X. Peng, H.T. Xu, Y. Shao, Z. Peng, K.F. Yao, Structures and corrosion properties of the $AlCrFeNiMo_{0.5}Ti_x$ high entropy alloys, Mater. Corros. 69 (2018) 641–647.
[54] Y.J. Hsu, W.C. Chiang, J.K. Wu, Corrosion behavior of $FeCoNiCrCu_x$ high-entropy alloys in 3.5% sodium chloride solution, Mater. Chem. Phys. 92 (2005) 112–117.
[55] J.M. Li, X. Yang, R.L. Zhu, Y. Zhang, Corrosion and serration behaviors of $TiZr_{0.5}NbCr_{0.5}V_xMo_y$ high entropy alloys in aqueous environments, Metals 4 (2014) 597–608.
[56] V. Soare, D. Mitrica, I. Constantin, V. Badilita, F. Stoiciu, A.-M. Popescu, I. Carcea, Influence of remelting on microstructure, hardness and corrosion behaviour of AlCoCrFeNiTi high entropy alloy, Mater. Sci. Technol. 31 (2015) 1194–1200.
[57] X.L. Yan, H. Guo, W. Yang, S.J. Pang, Q. Wang, Y. Liu, P.K. Liaw, T. Zhang, $Al_{0.3}Cr_x$FeCoNi high-entropy alloys with high corrosion resistance and good mechanical properties, J. Alloy. Compd. 860 (2021) 158436.
[58] P.C. Cui, Z.J. Bao, Y. Liu, F. Zhou, Z.H. Lai, Y. Zhou, J.C. Zhu, Corrosion behavior and mechanism of dual phase Fe1.125Ni1.06CrAl high entropy alloy, Corros. Sci. 201 (2022) 110276.
[59] C.W. Ji, A.B. Ma, J.H. Jiang, Mechanical properties and corrosion behavior of novel Al-Mg-Zn-Cu-Si lightweight high entropy alloys, J. Alloy. Compd. 900 (2022) 163508.
[60] P. Varshney, R.S. Mishra, N. Kumar, Understanding the nature of passivation film formed during corrosion of $Fe_{39}Mn_{20}Co_{20}Cr_{15}Si_5Al_1$ high entropy alloy in 3.5 wt% NaCl solution, J. Alloy. Compd. 904 (2022) 164100.
[61] M. Costa, C.-K. Peng, A.L. Goldberger, J.M. Hausdorff, Multiscale entropy analysis of human gait dynamics, Phys. A 330 (2003) 53–60.
[62] A. Crespo, D. Álvarez, G.C. Gutiérrez-Tobal, F. Vaquerizo-Villar, V. Barroso-García, M.L. Alonso-Álvarez, J. Terán-Santos, R. Hornero, Fd Campo, Multiscale entropy analysis of unattended oximetric recordings to assist in the screening of paediatric sleep apnoea at home, Entropy 19 (2017) 284.
[63] J. Qu, 8.06 - Thermomechanical reliability of microelectronic packaging, in: I. Milne, R.O. Ritchie, B. Karihaloo (Eds.), Comprehensive Structural Integrity, Pergamon, Oxford, 2003, pp. 219–239.
[64] G.T. Burstein, C. Liu, R.M. Souto, S.P. Vines, Origins of pitting corrosion, Corros. Eng. Sci. Technol. 39 (2004) 25–30.

CORRECTED PROOF